ADVANCED FUNCTIONAL MATERIALS

Supporting Information

for *Adv. Funct. Mater.,* DOI: 10.1002/adfm.202202157

Towards Low Cost and Sustainable Thin Film Thermoelectric Devices Based on Quaternary Chalcogenides

*Eleonora Isotta, Jacob Andrade-Arvizu, Ubaidah Syafiq, Alex Jiménez-Arguijo, Alejandro Navarro-Güell, Maxim Guc, Edgardo Saucedo, and Paolo Scardi**

Towards low cost and sustainable thin film thermoelectric devices based on Cu-rich Cu_2ZnSnS_4 and $Cu_2ZnSnSe_4$

Eleonora Isotta[1], Jacob Andrade-Arvizu[2], Ubaidah Syafiq[1,3], Alex Jiménez-Arguijo[2,4], Alejandro Navarro-Güell[4], Maxim Guc[2], Edgardo Saucedo[4], and Paolo Scardi[1,*]

[1] Department of Civil, Environmental and Mechanical Engineering, University of Trento, Italy
[2] Solar Energy Materials and Systems Group, Catalonia Institute for Energy Research (IREC), Barcelona, Spain
[3] Solar Energy Research Institute, the National University of Malaysia (SERI-UKM), 43600 Bangi, Selangor, Malaysia
[4] Photovoltaic Group, Electronic Engineering Department, Polytechnic University of Catalonia (UPC), Barcelona, Spain
*Author to whom correspondence should be addressed: paolo.scardi@unitn.it

Supplementary Information

Thermal profile for the chalcogenization of CZTS and CZTSe

The thermal profiles are shown in Figure S1 and are summarized as following.

CZTS: two-step thermal profile. Ramps of 20 ˚C/min. First step with dwelling time of 15 min and at 250˚C with an Ar flux of 1 mbar. Second step with dwelling time of 30 min at 570˚C with an Ar static pressure of 950 mbar[1].

CZTSe: two-step thermal profile. Ramps of 20 ˚C/min. First step with dwelling time of 30 min and at 400˚C with an Ar flux of 1.5 mbar. Second step with dwelling time of 30 min at 550˚C with an Ar static pressure of 950 mbar[2].

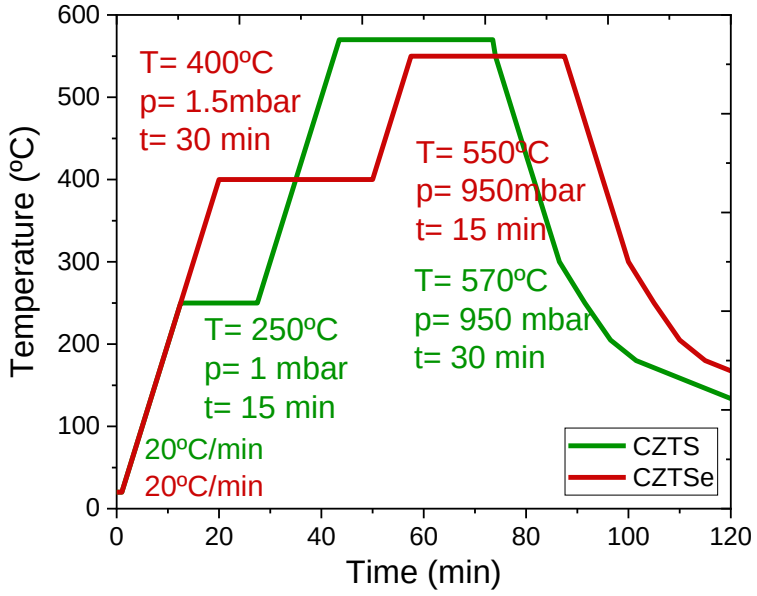

Figure S1. Thermal profiles for the chalcogenization of CZTS and CZTSe thin film samples.

Further details from XRD

A Rietveld refinement of X-Ray Diffraction data was performed with the software TOPAS 7[3], with the aid of whole powder pattern modelling[4] (WPPM) macros[5] for the analysis of crystal domain size and strain. Refinement results can be seen in Table 1, while an example of refinement is reported in Figure S2, on a CZTS thin film sample.

	Space group	Lattice parameters [Å]	Domain size LVol [nm]	Microstrain e_0 [-]	B_{iso} [Å^2]
CZTS	*I*-42*m*	a = 5.4261 c = 10.8316	460	0.00012	Cations: 2 S: 0.6
CZTSe	*I*-42*m*	a = 5.6879 c = 11.3485	640	0.0005	Cations: 1.6 Se: 0.4
AZO	$P6_3mc$	a = 3.2642 c = 5.2348	640	0.001	Al/Zn: 1 O: 1

Table 1. Refinement parameters obtained from the Rietveld analysis of X-ray diffraction data.

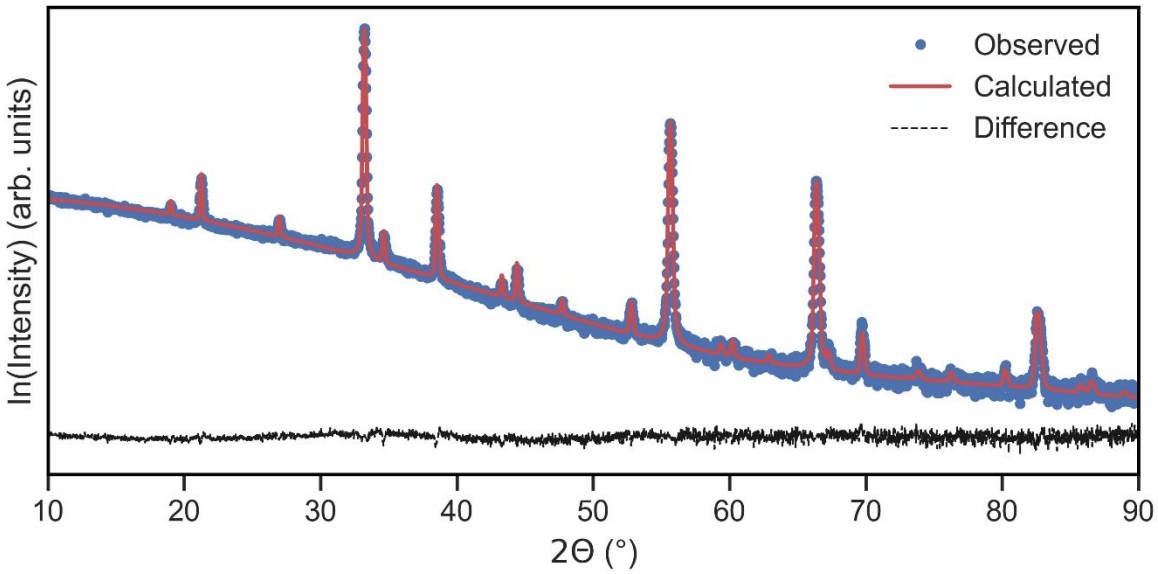

Figure S2. Example of Rietveld refinement of X-ray diffraction data performed on thin film a sample of CZTS.

Additional Scanning Electron Microscopy (SEM) images

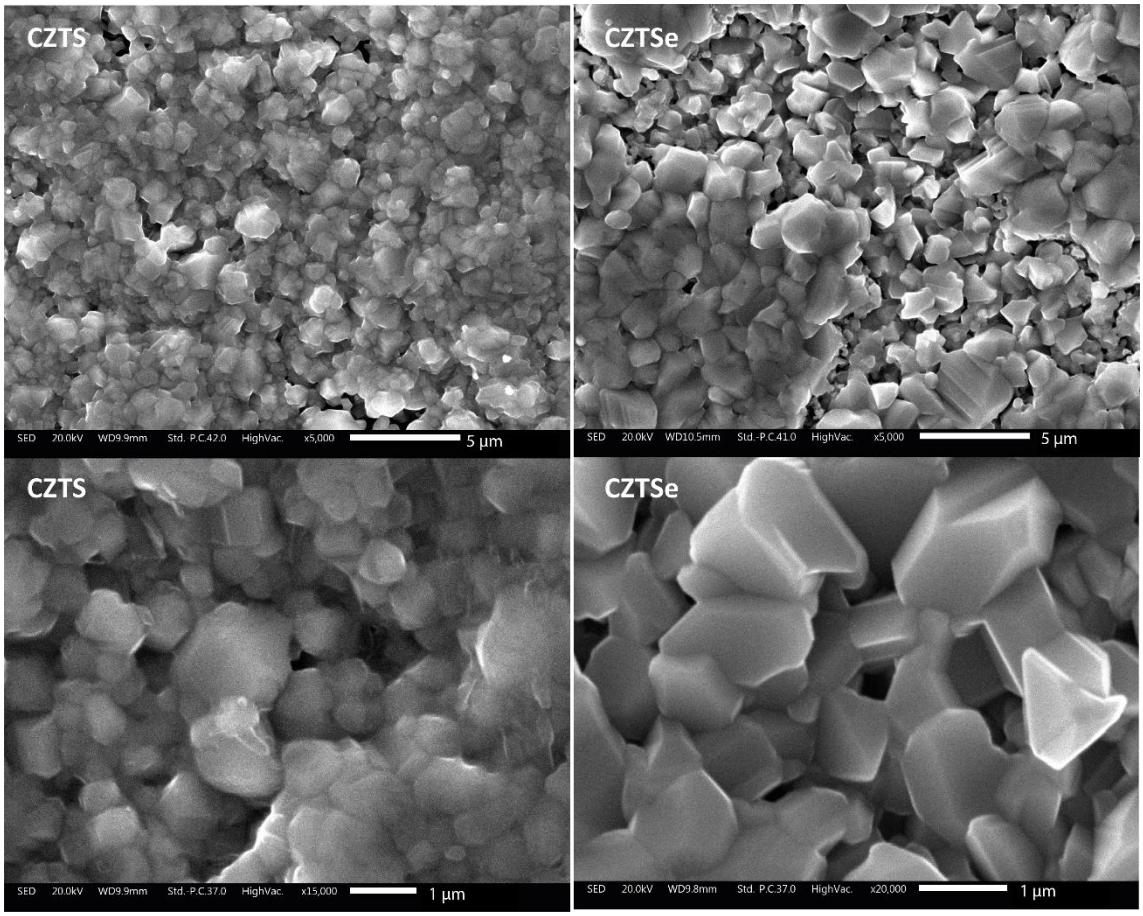

Figure S3. Scanning electron microscopy images collected on the surface of a CZTS and a CZTSe thin film samples.

Compositional mapping

EDS maps are shown in Figure S4 and S5. As visible, elements result being evenly distributed. The darker shadows present the same pattern for all the elements, indicating they are caused by the surface morphology shown in the "Grey" image.

As a further proof, X-ray Fluorescence (XRF) was measured with a Fischerscope XVD-SDD system on 9 different points (on a 3x3 grid across a sample area of 2.5 cm x 2.5 cm) for 45 s each. Results are visible in Table 2 and 3 and indicate a uniform distribution of all the elements.

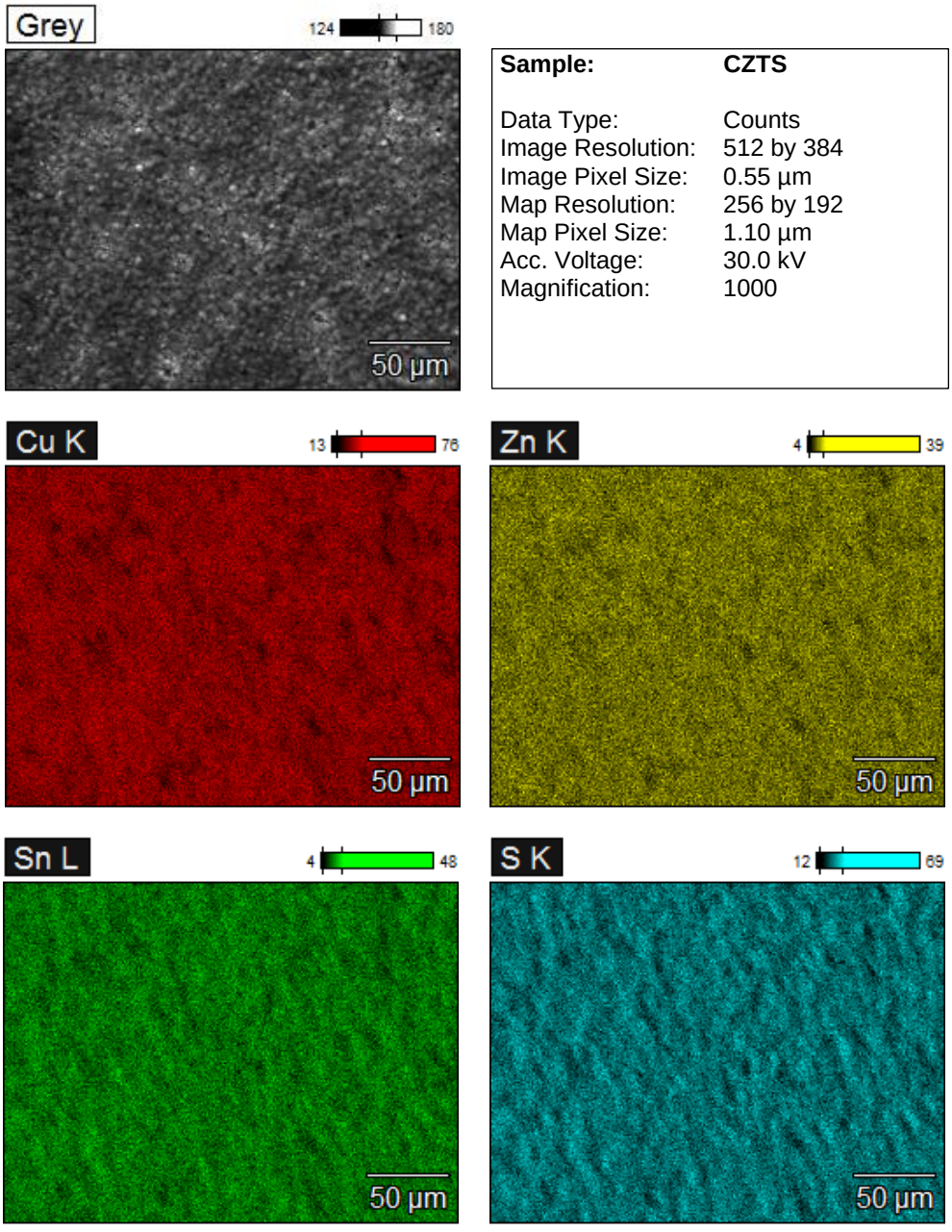

Figure S4. EDS maps showing the elemental distribution for a thin film sample of CZTS.

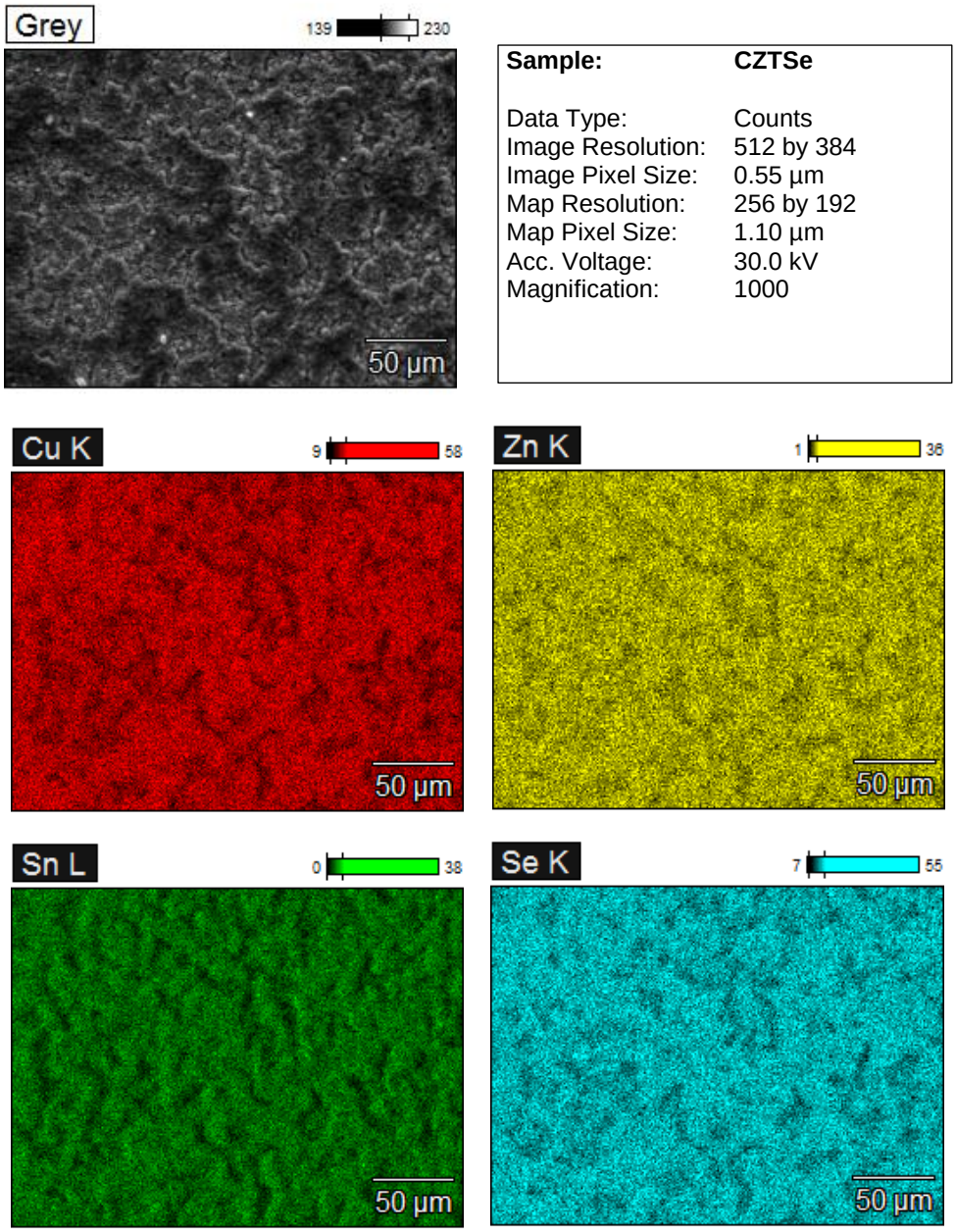

Figure S5. EDS maps showing the elemental distribution for a thin film sample of CZTSe.

	Cu [%w]	Zn [%w]	Sn [%w]	Se [%w]
CZTSe point 1	25.8	10.2	13.7	50.2
CZTSe point 2	25.6	10.2	13.6	50.5
CZTSe point 3	25.8	10.2	13.7	50.4
CZTSe point 4	25.5	10.3	14	50.2
CZTSe point 5	25.7	10.3	13.8	50.2
CZTSe point 6	25.6	10.3	13.4	50.7
CZTSe point 7	25.7	10.2	13.8	50.3
CZTSe point 8	25.9	10.2	13.5	50.4
CZTSe point 9	25.6	10.3	13.8	50.4

Table 2. Results of the XRF spectra collected at 9 different locations over a 2.5cm x 2.5 cm CZTSe sample area.

	Cu [%w]	Zn [%w]	Sn [%w]	S [%w]
CZTS point 1	26.9	12.8	15.1	45.1
CZTS point 2	27	12.8	14.9	45.3
CZTS point 3	27.3	12.8	15.1	44.8
CZTS point 4	27.2	12.9	14.9	45
CZTS point 5	27.2	13	14.9	44.9
CZTS point 6	27.3	13	14.9	44.8
CZTS point 7	26.6	12.7	15	45.7
CZTS point 8	27.4	13	15.2	44.3
CZTS point 9	27.3	13	15	44.7

Table 3. Results of the XRF spectra collected at 9 different locations over a 2.5cm x 2.5 cm CZTS sample area.

UV-Vis characterization

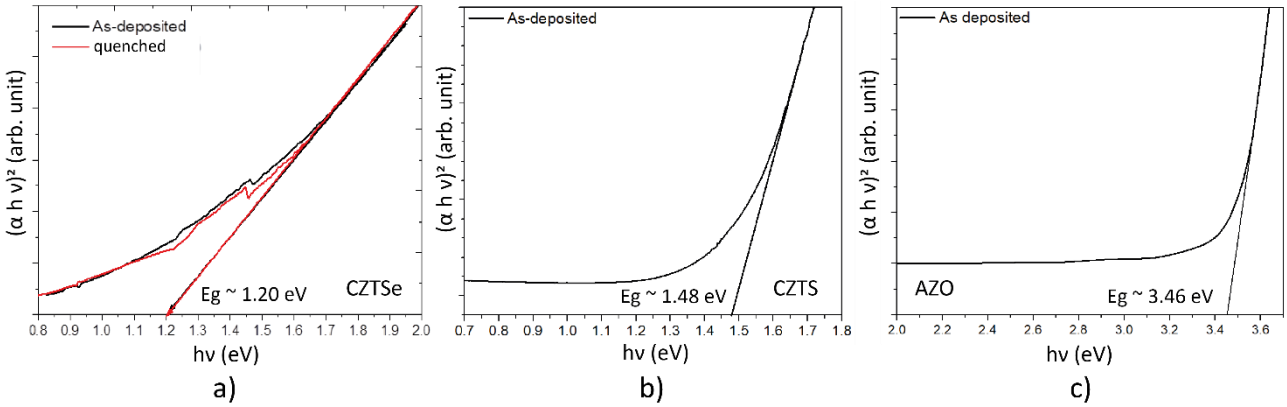

Figure S6. UV-Vis spectroscopy performed on thin film samples of CZTSe, as-deposited and quenched (a), CZTS (b) and AZO (c). The value of the bandgap Eg has been extrapolated from the linear part of the Tauc's plot

Raman spectroscopy on quenched samples

Both CZTS and CZTSe are reported to face a reversible order-disorder phase transition, at 260 ± 10°C for the sulphur[6] and 200 ± 20°C for the selenium[7] compounds. This features a randomization of the Cu and Zn occupancy in the intermediate planes of ordered *I-4* kesterite, thus transitioning to the *I-42m* space group or disordered kesterite structure[8]. In order to investigate the potential extent of these transitions upon exposure to high temperatures, Raman spectra were collected on samples of CZTS and CZTSe quenched from 275°C and 230°C, respectively (**Error! Reference source not found.**b-c, solid red lines and insets).

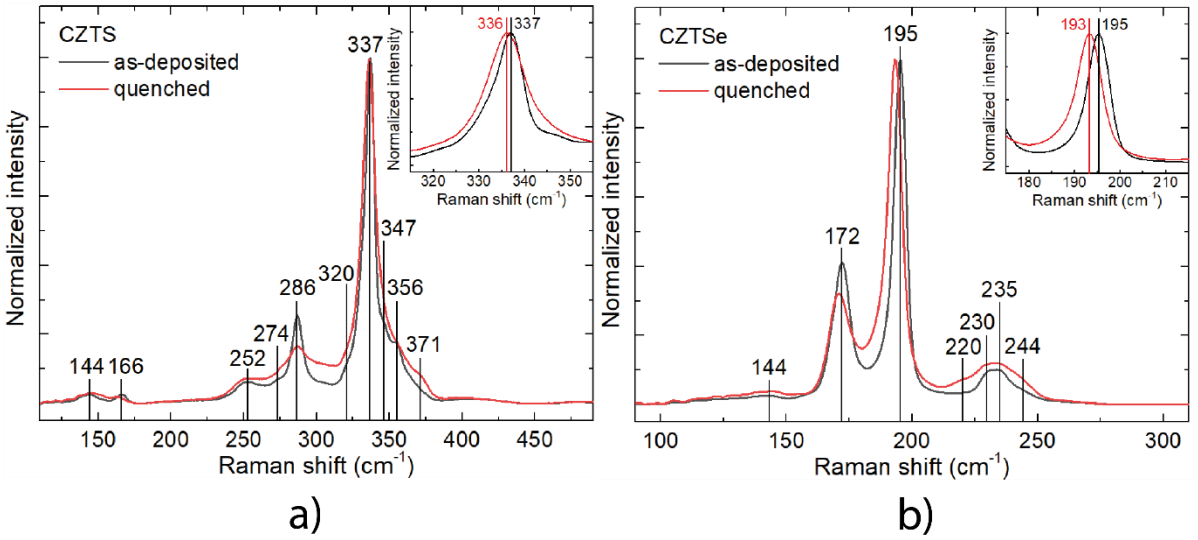

Figure S7. Raman spectra for a Cu-doped CZTS and Cu-doped CZTSe as deposited and after a quenching step. This was intended to understand the extent of the Cu-Zn disorder during in-temperature operations of the materials and confirm the occurrence of order-disorder phenomena.

These indicate that Cu-Zn order-disorder phenomena are at place. Indeed, after quenching there is a clear redshift and increased asymmetry of the peaks. Both effects, together with the decrease in intensity of the second Raman band (at 286 and 172 cm^{-1} for CZTS and CZTSe, respectively), are attributed to the increased Cu-Zn disordering[7,9]

Setup for the measurement of in-plane Seebeck coefficient and electrical resistivity on thin films

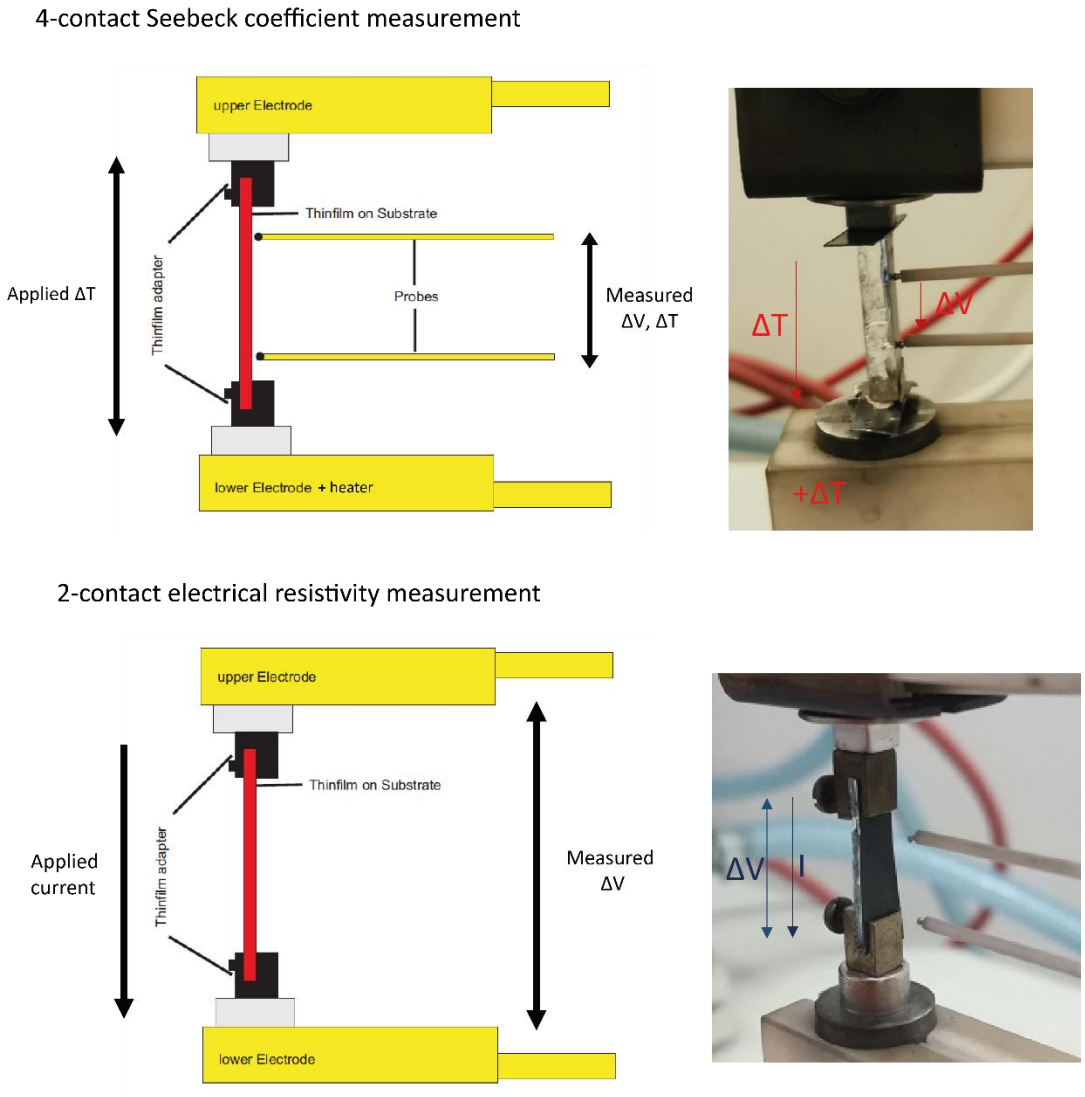

Figure S8. Setup for the measurement of in-plane Seebeck coefficient(4-contact) and in-plane electrical resistivity (2-contact) on thin film samples. The samples were mounted on a Linseis LSR-3 with the aid of a thin film adapter.

Verification of thermoelectric measurements

To verify the reliability of measurements performed on the Linseis LSR-3 setup, adapted for hosting thin film samples, results were checked with alternative methods. The electrical resistivity ρ was measured also with a standard laboratory multimeter on individual legs, using geometrical width, thickness, and length of the legs. Additionally, ρ was measured on the deposited samples with a 4-point probe setup. Results are visible in Table 4, and are reasonably in accordance with what measured with the Linseis LSR-3 setup.

	Thickness profilometer [µm]	ρ 2-contact multimeter [µΩ*m]	ρ 4-point probe [µΩ*m]
CZTS	2.5	376	225
CZTSe	3	41	42
AZO	0.25	19.6	11.2

Table 4. Thickness and electrical resistivity for a CZTS, CZTSe and AZO thin film samples. Results were obtained, respectively, with a profilometer, with a multimeter in 2-contact configuration and with a 4-point probe. Reasonable matching is found with the result measure d on the Linseis LSR-3 setup.

The Seebeck coefficient was verified mounting samples with scratched contacts (see Figure S9a) on the TEG test setup. This allows the measurement of the open circuit voltage produced by individual legs. Through a thermal camera measurement of the temperature gradient across the leg (Figure S9b), it is possible to estimate the Seebeck coefficient as $S = V_{oc}/\Delta T$. As an example, measurement conditions and values for a CZTSe/AZO device can be seen in Figure S5. Results are found in good agreement with respect to what measured on the Linseis LSR-3 setup.

Additionally, no major contributions to the V_{oc} seem to arise from the metal contacts, nor from the p-n junctions, as the sum of the voltages produced from the individual legs is found matching with the V_{oc} of the unscratched TEG device.

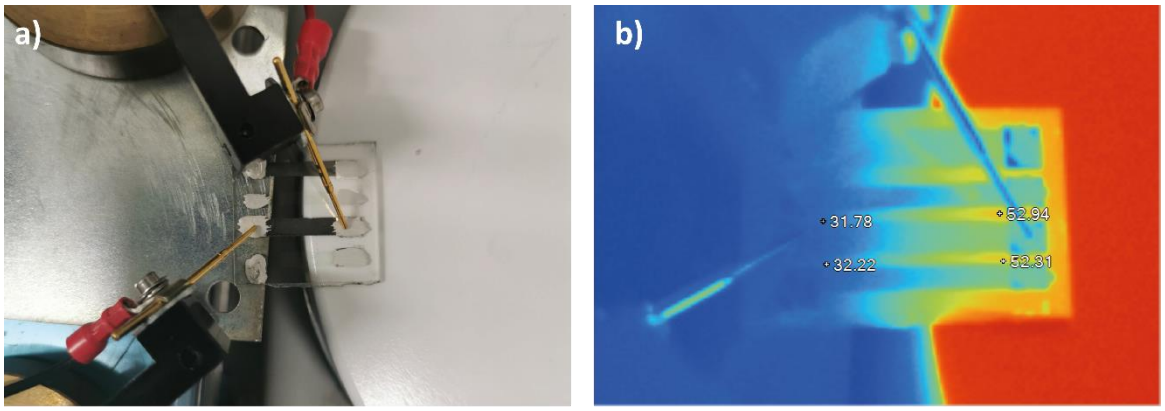

c)

	V_{OC} [mV]	ΔT [K]	S_{est} [µV/K]	S_{LSR-3} [µV/K]
AZO 1	0,942	25	-38	-40
CZTSe 1	-1,864	20,6	90	78
AZO 2	0,693	19,6	-35	-40
CZTSe 2	-2,312	24,9	93	78
Sum	5,811			
Unscratched whole TEG	5,804 *			

* little contribution of pn junction, contacts..

Figure S9. a) CZTSe/AZO TEG device with scratched contacts in order to measure the contribution of individual legs. b) Thermal camera image probing the temperature difference ΔT during the measurement of open circuit voltage Voc on individual legs. c) Table summarizing the results of the individual leg test on the TEG test setup. The Seebeck coefficient estimated in this way, S_{est}, in reasonably in agreement with what has been measured on the Linseis LSR-3 setup, S_{LSR-3}.

Electronic properties of AZO from different region of the substrate

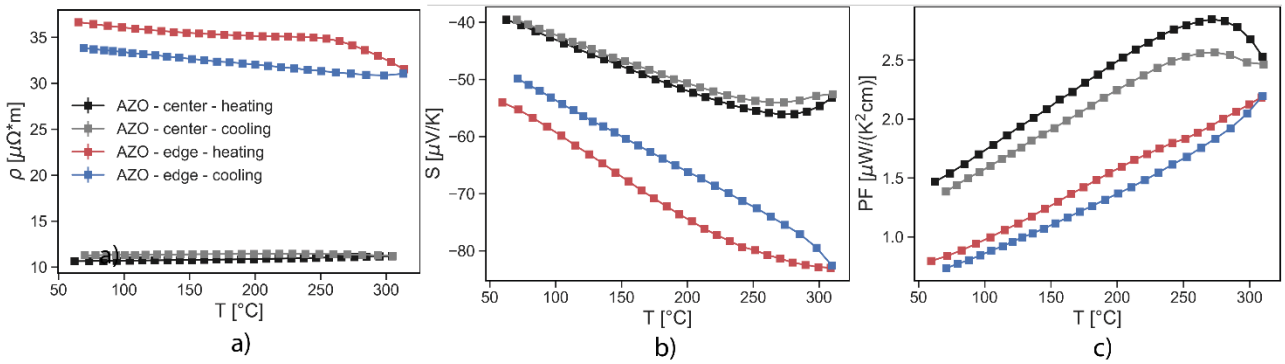

Figure S10. Electrical resistivity ρ, Seebeck coefficient S and power factor PF for two samples of AZO: one cut from the central area of the deposited film, and one cut from the edge. As visible, the sample cut from the marginal area presents higher absolute values of electrical resistivity and Seebeck coefficient, as well as greater instability of the results over the heating and cooling cycles.

Raman spectroscopy (**Error! Reference source not found.**d in the main text) pointed to compositional inhomogeneities in AZO depositions, known to cause differences in electrical resistivity. It was indeed verified, as visible in Figure S10 that samples cut from the marginal areas of the sputtered batch presented a higher ρ, as well as a higher absolute value of Seebeck coefficient. To overcome this issue, whenever the ρ of n-type legs was found larger than expected, an additional layer of AZO was sputtered to match the required leg resistance.

Optimization of TEG devices

The optimization of TEG devices described in the main text has been performed optimizing the following equation of a device ZT.

$$ZT = \frac{(S_p - S_n)^2}{K\,R}\,T, \qquad \text{Minimize } KR = \left(\frac{\rho_P}{w_P t_P} + \frac{\rho_n}{w_n t_n}\right) * \left(\kappa_p w_p t_p + \kappa_n w_n t_n + \kappa_g w_g t_g\right)$$

where t and w stands for thickness and width, while the subscripts p, n, g stand for p-type leg, n-type leg, and SLG substrate, respectively.

The input parameters for the minimization can be seen in Table 5.

	Thickness [μm]	**Electrical resistivity ρ [μΩ*m]**	**Thermal conductivity [W/(mK)]**	**Width [mm]**
CZTS	2.6 (measured)	410 (measured)	2.8 (Ref [10])	2 (optimized)
AZO	0.250 (measured)	10.7 (measured)	4.5 (Ref [11])	2.5 (fixed)
CZTSe	3 (measured)	46 (measured)	3.75 (Ref [10])	1.5 (optimized)
AZO	0.250 (measured)	10.7 (measured)	4.5 (Ref [11])	3 (fixed)
SLG substrate	1000 (measured)	-	1 (Ref [12])	$w_p + w_n + 1$

Table 5. Input and output parameters for the optimization of the relative p to n width of legs in the CZTS/AZO and CZTSe/AZO TEG devices.

The leg length was designed and considered equal for all the elements, while the thickness was kept fixed to the values known to provide consistent compositional results according to the specific deposition method. The values of electrical resistivity have been taken from the room temperature measurements performed on the Linsies LSR-3. The values of thermal conductivity have been taken from the literature [10–12].

In Figure S11, minimization plots are shown, illustrating the optimal width of the p type legs, once the width of the n legs was fixed. In the choice, the smallest width that minimizes the curve has been chosen, in the sake of having a smaller device area and therefore a higher power per unit area.

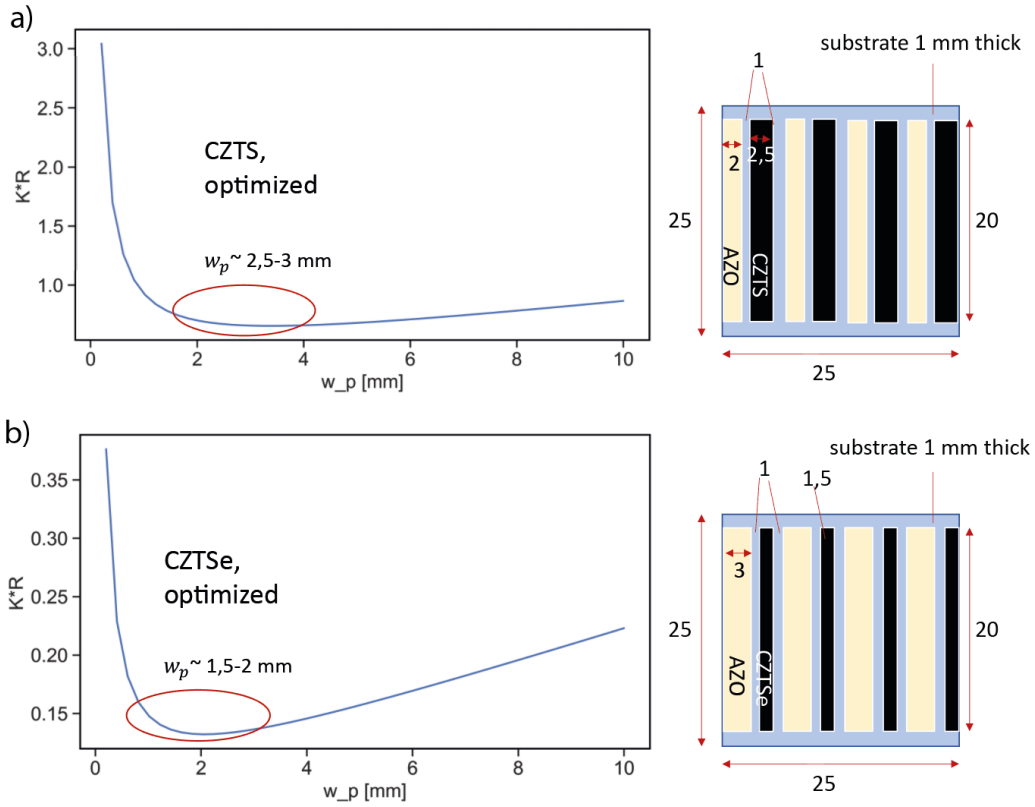

Figure S11. Result of the optimization of the relative leg width for a CZTS/AZO (a) and a CZTSe/AZO TEG devices. On the right side, a schematic picture of the optimized devices is reported.

TEG performance upon cycling

In Figure S12, results of cycling on the IP curves are presented. CZTS-based devices show the greater degradation of performance under repeated measurements, with peak power values dropping of ~40% after three cycles. This is noticed coming from an increase in resistance of the CZTS legs (overall device internal resistance increasing from 2.7 kΩ before the measurements, to 4.48 kΩ after the measurements) suggesting that, for practical applications, they would require a suitable coating to prevent oxidation and material degradation. CZTSe-based devices, show instead a much higher stability of results over cycling, with the power maintaining more than ~75% of the original peak value after 7 measurements. For this case, it is not noticed a general and constant decrease of performance with cycling but rather fluctuating values. This is believed connected with the measurement temperature being above the order-disorder transition one. In fact, this might cause a partial quenching of the p-type material to the disorder phase, observed to yield a greater power factor (**Error! Reference source not found.**f). As a proof of concept, the CZTSe optimized device was quenched from a temperature of 230°C after the first measurement, and indeed yielded improved results, of more than the 15%. The cycling has then been performed successively.

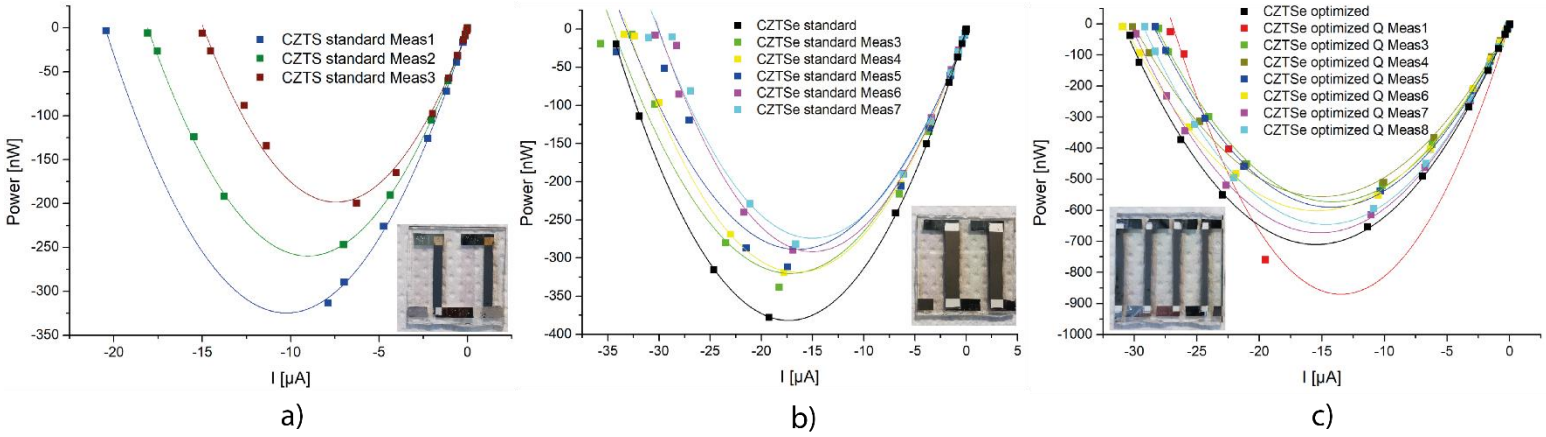

Figure S12. Result of repeated IVP measurements performed on a standard TEG device CZTS/AZO (a), standard CZTSe/AZO (b) and optimized CZTSe/AZO (c). The latter, after the first measurement has been quenched from a temperature of 230°C (notation "Q" in the label), and then repeatedly measured.

References

1 E. Ojeda-Durán, K. Monfil-Leyva, J. Andrade-Arvizu, I. Becerril-Romero, Y. Sánchez, R. Fonoll-Rubio, M. Guc, Z. J. Li-Kao, J. A. Luna-López and E. Saucedo, *J. Mater. Chem. C*, 2021, **9**, 5356–5361.

2 S. Giraldo, E. Saucedo, M. Neuschitzer, F. Oliva, M. Placidi, X. Alcobé, V. Izquierdo-Roca, S. Kim, H. Tampo, H. Shibata, A. Pérez-Rodríguez and P. Pistor, *Energy Environ. Sci.*, 2018, **11**, 582–593.

3 A. A. Coelho, *J. Appl. Crystallogr.*, 2018, **51**, 210–218.

4 P. Scardi and M. Leoni, *Acta Crystallogr. Sect. A Found. Crystallogr.*, 2002, **58**, 190–200.

5 P. Scardi, C. L. Azanza Ricardo, C. Perez-Demydenko and A. A. Coelho, *J. Appl. Crystallogr.*, 2018, **51**, 1752–1765.

6 J. J. S. Scragg, L. Choubrac, A. Lafond, T. Ericson and C. Platzer-Björkman, *Appl. Phys. Lett.*, 2014, **104**, 041911.

7 G. Rey, A. Redinger, J. Sendler, T. P. Weiss, M. Thevenin, M. Guennou, B. El Adib and S. Siebentritt, *Appl. Phys. Lett.*, , DOI:10.1063/1.4896315.

8 S. Schorr and G. Gonzalez-Aviles, *Phys. Status Solidi Appl. Mater. Sci.*, 2009, **206**, 1054–1058.

9 M. Y. Valakh, O. F. Kolomys, S. S. Ponomaryov, V. O. Yukhymchuk, I. S. Babichuk, V. Izquierdo-Roca, E. Saucedo, A. Perez-Rodriguez, J. R. Morante, S. Schorr and I. V. Bodnar, *Phys. Status Solidi - Rapid Res. Lett.*, 2013, **7**, 258–261.

10 M. L. Liu, F. Q. Huang, L. D. Chen and I. W. Chen, *Appl. Phys. Lett.*, 2009, **94**, 202103.

11 U. Syafiq, E. Isotta, N. Ataollahi, K. Lohani, S. Luong, V. Trifiletti, O. Fenwick and P. Scardi, *Submitted*.

12 S. M. Karazi, I. U. Ahad and K. Y. Benyounis, *Ref. Modul. Mater. Sci. Mater. Eng.*, , DOI:10.1016/b978-0-12-803581-8.04149-7.